# Integration of epitaxial LiNbO<sub>3</sub> thin films with silicon technology

Ausrine Bartasyte<sup>1,2</sup>, Stefania Oliveri<sup>1</sup>, Sondes Boujnah<sup>1</sup>, Samuel Margueron<sup>1</sup>, Romain Bachelet<sup>3</sup>, Guillaume Saint-Girons<sup>3</sup>, David Albertini<sup>4</sup>, Brice Gautier<sup>4</sup>, Pascal Boulet<sup>5</sup>, Ioana Nuta<sup>6</sup>, Elisabeth Blanquet<sup>6</sup>, Vincent Astié<sup>7</sup>, and Jean-Manuel Decams<sup>7</sup>

- <sup>1</sup> FEMTO-ST Institute, University of Franche-Comté, CNRS (UMR 6174), ENSMM, Besançon, France
- <sup>2</sup> Institut Universitaire de France, Paris, France
- <sup>3</sup> Université de Lyon, Ecole centrale de Lyon, INL, Ecully cedex, France
- <sup>4</sup> Université de Lyon, INSA de Lyon, INL, Villeurbanne, France
- <sup>5</sup> Jean Lamour Institute, CNRS (UMR 7198), University of Lorraine, Nancy, France
- <sup>6</sup> SIMAP, Université Grenoble Alpes, CNRS (UMR 5266), Saint Martin d'Hères, France

E-mail: ausrine.bartasyte@femto-st.fr

Received xxxxxx Accepted for publication xxxxxx Published xxxxxx

#### **Abstract**

Development of bulk acoustic wave filters with ultra-wide pass bands and operating at high frequencies for 5<sup>th</sup> and 6<sup>th</sup> generation telecommunication applications and micro-scale actuators, energy harvesters and sensors requires lead-free piezoelectric thin films with high electromechanical coupling and compatible with Si technology. In this paper, the epitaxial growth of 36°Y-X and 30°X-Y LiNbO<sub>3</sub> films by direct liquid injection chemical vapour deposition on Si substrates by using epitaxial SrTiO<sub>3</sub> layers, grown by molecular beam epitaxy, has been demonstrated. The stability of the interfaces and chemical interactions between SrTiO<sub>3</sub>, LiNbO<sub>3</sub> and Si were studied experimentally and by thermodynamical calculations. The experimental conditions for pure 36°Y-X orientation growth have been optimized. The piezoelectricity of epitaxial 36°Y-LiNbO<sub>3</sub>/SrTiO<sub>3</sub>/Si films was confirmed by means of piezoelectric force microscopy measurements and the ferroelectric domain inversion was attained at 85 kV.cm<sup>-1</sup> as expected for the nearly stoichiometric LiNbO<sub>3</sub>. According to the theoretical calculations, 36°Y-X LiNbO<sub>3</sub> films on Si could offer an electromechanical coupling of 24.4 % for thickness extension excitation of bulk acoustic waves and a comparable figure of merit of actuators and vibrational energy harvesters to that of standard PbZr<sub>1-x</sub>Ti<sub>x</sub>O<sub>3</sub> films.

Keywords: LiNbO3 films, epitaxy, silicon, CVD, MBE, BAW, electro-active devices

### 1. Introduction

Radio frequency (RF) acoustic filters based on piezoelectric materials are widely used in the field of telecommunication (smartphones, tablets, data treatment, Wi-Fi, DSL, Bluetooth, GPS devices, etc.). To intensify the transmission of data (dynamic images, sound, internet, database...), the number of RF bands dedicated to

transmission of data, the width of the pass band and/or the working frequency have to be increased. This motivates the development of filters with ultra-wide pass bands and operating at much higher frequencies going up to 24 GHz for 5G and 6G applications [1,2]. The RF filter technologies rely on surface acoustic wave (SAW) and bulk acoustic wave (BAW) devices based on piezoelectric materials such as LiNbO<sub>3</sub> (LN) & LiTaO<sub>3</sub> (LT) single-crystal wafers and piezoelectric AlN thin films on electrode/(Bragg mirror or

<sup>&</sup>lt;sup>7</sup> Annealsys, Montpellier, France

sacrificial layer)/SiO<sub>2</sub>/Si substrates, respectively. In the case of high-frequency applications, BAW filters are preferred due to their ability to withstand high power density. In order to be applied in wide-band BAW filters, a piezoelectric material must have high electromechanical coupling for the thickness mode (mainly based on longitudinal waves although shear waves could also be used),  $K_t^2$ , and high-quality factor, Q. AlN films present high quality factor (2490 at 2 GHz) but their  $K_t^2$  of longitudinal mode is limited to 6.5 % [3].

Therefore, the BAW filters based on AlN are limited to frequencies up to 4 GHz, due to too narrow achievable bandwidth at higher frequencies. Recently, it was demonstrated an electromechanical coupling increased by a factor of two in mixed Al<sub>1-x</sub>Sc<sub>x</sub>N (AlScN) solutions compared to that of AlN [4,5]. Nevertheless, the acoustical performance of AlScN films is not sufficient to attain the reasonable bandwidths of filters operating at/above 6 GHz. LN crystals presents several orientations (defined according to IEEE Std-176 convention [6]) showing BAW modes with high electromechanical coupling, K<sup>2</sup>: 163° rotated-Y cut (38%), 36°Y-LN (25%), and X-LN (46%) [7]. A K<sup>2</sup> of 53 % has been demonstrated for BAW devices based on X-cut LN films fabricated by ion slicing [8]. Translated in terms of filters, this means a BAW RF filter based on LN could present several times broader pass band than that based on AlN films [9]. At present, the techniques enabling the fabrication of BAW devices based on single crystalline LN thin films with required orientation are polishing or crystal ion slicing and wafer bonding techniques. The polishing techniques induce a large material consumption since a LN wafer needs to be grinded down to leave only a thin film remaining. Ion slicing remains relatively expensive technique as compared to the standard thin film deposition methods. The main factors defining BAW frequency are the piezoelectric film thickness and the phase velocity although other factors such as metal mass, used for electrodes, and layers, used to compensate the temperature coefficient of frequency, also play a role. Both top-down techniques include polishing steps which introduces difficulties in the film thickness homogeneity and in consequence the imprecision in the frequency control. Moreover, the lowest thickness which can be attained by ion slicing is 300 nm. This limits the highest attainable BAW frequency with longitudinal wave velocity of around 5000 m/s to around 8.3 GHz [10].

Energy harvesting in combination with ultra-low power electronics are urgently needed for the implementation of self-powered sensors for the internet of things, health monitoring and more generally 4.0 industry [11,12]. Pb-containing piezoelectric materials, such as PbZr<sub>1-x</sub>Ti<sub>x</sub>O<sub>3</sub> (PZT) ceramics or thin films, are usually considered as the best performing electromechanical transducers. According to REACH and RoHs regulations in EU, the lead-free materials have to be considered for these applications. Recently, it was

demonstrated that single-crystal LN films may offer a comparable performance in terms of vibrational energy harvesting at meso-scale to that of PZT [13]. This indicates a particular interest in deposited LN films for MEMS-scale actuators, energy harvesters and sensors [14].

Despite the high industrial interest in LN films, the deposition methods of these films are still far from being a routine [15]. The formation of silicates and the presence of amorphous SiO<sub>2</sub> at the interface between LN and Si induce polycrystallinity of the grown layers directly grown on Si in most of the reported results. Polycrystalline films do not present any real potential in acoustic wave or electro-active applications. Z- LN films were obtained on heterostructures consisting of textured buffers layers (ZnO, Pt, etc.) [15] or epitaxial Y<sub>2</sub>O<sub>3</sub> films on Si substrates [16], respectively. TFBAR (thin film bulk acoustic resonator) and Lamb wave devices were fabricated using Z-LN films grown on ZnO buffer layer on LN substrate for the fabrication of LN membranes by wet etching of ZnO [17,18]. Z-orientation of LN shows similar  $K_t^2$  to that of AlN films [17], thus from the industrial point of view Z-LN films do not present any particular interest in the BAW filters. In order to attain high electromechanical coupling of thickness extensional mode, high-quality LN films with oblique Z-axis (c-axis) or X-axis (a-axis,  $(11\overline{2}0)$  orientation) need to be grown on the heterostructures compatible with large-scale BAW fabrication techniques. The comparable figure of merit of vibrational energy harvesting or actuation to that of PZT films can be obtained by using  $(01\overline{1}2)$  LN orientation [14].

Epitaxial growth of (1120) and (0112) LN films is relatively well described in literature on sapphire substrates [15]. Single-crystal (pseudo)cubic substrates such as SrTiO<sub>3</sub>, LaAlO<sub>3</sub>, NdGaO<sub>3</sub>, MgO, etc. were used to grow (0112) LN films [15]. However, these substrates are not compatible with industrial fabrication. So far these highly coupled LN orientations of deposited LN films were not explored for BAW devices or other electro-active applications.

In this work, epitaxial (0112) and (1123) LN films (offering oblique orientation of polarization axis) were grown by direct liquid injection chemical vapour deposition (DLI-CVD) on Si with epitaxial SrTiO<sub>3</sub> (STO) buffer layer, obtained by molecular beam epitaxy (MBE). The films were investigated by means of X-ray diffraction (XRD), Raman spectroscopy (RS) and piezoelectric force microscopy (PFM). The study of chemical interactions between STO, LN and Si was supported by thermodynamical calculations. The electromechanical coupling of thickness extension excitation for BAW devices and figure of merit for vibrational energy harvesters and actuators were calculated for these two epitaxially grown orientations and compared to those of standard c-axis oriented LN films.

## 2. Experimental details

Epitaxial (100) oriented STO layers with thicknesses of 25 nm and 50 nm were grown on (100) Si substrates by MBE. The thicknesses of STO layers were measured by means of Xray Reflectivity (XRR). Typically, the roughness of STO/Si tempelates are below 1 nm [19] and the detailed description of STO deposition process can be found elsewhere [19,20]. The structural quality of STO surface was monitored during growth by in-situ reflection high-energy electron diffraction (RHEED) operating at 30 keV. The epitaxial LN films on STO/Si templates and STO, LaAlO<sub>3</sub> (LAO), (LaAlO<sub>3</sub>)<sub>0.3</sub>(Sr<sub>2</sub>TaAlO<sub>6</sub>)<sub>0.7</sub> (LSAT) single crystal substrates (supplied by MTIxtl) were deposited at deposition temperatures ranging from 600 °C to 750 °C by DLI-CVD. Li(tmhd) and Nb(tmhd)<sub>4</sub> (tmhd - tetramethylheptanedionate) precursors dissolved in mesitylene with orthophenanthroline as Lewis bases were used. More details about deposition conditions can be found. in Ref. [21] and [22]. Raman spectra in a crossed polarization configuration were collected by using an S&I MonoVista Raman spectrometer with excitation at 532 nm. Raman modes were identified according to the assignment given in Ref. [23]. The spectra were calibrated by measuring the spectra of 36°Y-X LN single crystal with congruent composition (48.34 mol\% of Li<sub>2</sub>O) for an equivalent polarization configuration. The linear relationship, %Li<sub>2</sub>O=55.01-0.66\*FWHM, between E(1TO) mode damping parameters, FWHM (full width at half maximum), and Li<sub>2</sub>O concentration within LN, %Li<sub>2</sub>O, was used to estimate the Li<sub>2</sub>O nonstoichiometry in the grown LN films by means of Raman spectroscopy analysis (more details can be found in Ref. [24]). The spectra were reduced by Bose distribution and fitted using independent damped harmonic oscillator spectral profiles and a linear baseline. The texture and epitaxial quality of grown films were studied by means of XRD.  $\Theta/2\Theta$  patterns were collected by using a Bruker D8 Advance diffractometer with monochromatic Cu  $K_{\alpha 1}$  radiation (1.54056 Å) or AERIS Panalytical diffractometer without monochromator. The rocking curves, φ-scans and pole figures were measured by Bruker D8 Discover diffractometer with Co Kα radiation (1.79026 Å). The chemical reactions between STO and LN were thermodynamically evaluated from their Gibbs energies and simulated through the Factsage software package [25]. The piezoelectricity and ferroelectric domain structure of LN films on STO/Si were studied by means of piezoelectric force microcopy (PFM). Vertical piezoresponse force microscopy (VPFM) and lateral PFM (LPFM) images were obtained with the Dual Frequency Resonance Tracking mode (DFRT). Standard Sawyer-Tower circuit was used to measure the coercive field of the transferred films.

## 3. Results

Two STO/Si templates with 25 nm (stoichiometric) and 50 nm (Sr-rich) thick STO layers were used for the epitaxial growth of LN films. RHEED patterns of the surface structure of these STO films are presented in Fig. 1 a and b, respectively. The 50 nm thick STO film presents SrO islands on the surface due to insufficient compensation of Sr-excess (required for early stage STO epitaxial growth) and of Sr surface segregation during thin film growth, while 25 nm thick STO film shows a chemically pure and flat STO surface. The full widths at half maximum (FWHM) of (200) STO rocking curves were 1.8° and 1.4°, respectively. The roughnesses of STO layers were 3.2 nm and 0.8 nm, respectively. A layer of SiOx with a thickness of 2.1 nm formed during the STO growth on Si. The 50 nm thick STO film had lattice parameter of 3.93 Å, while the lattice of 25 nm STO was slightly larger (3.94 Å) and presented gradient in the lattice spacings.

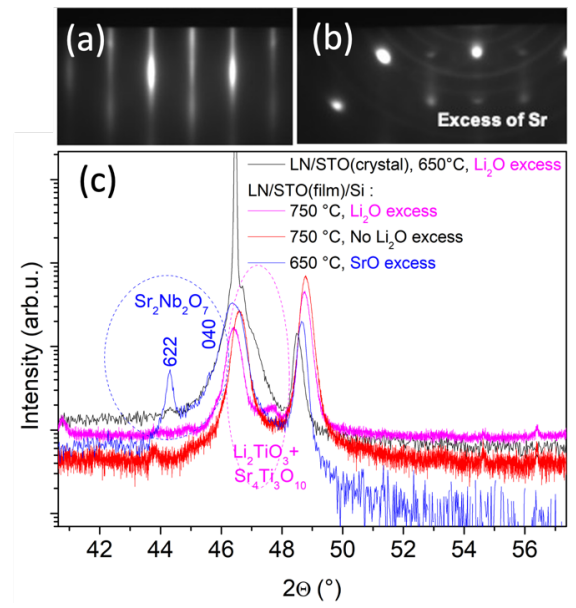


Figure 1. RHEED patterns of epitaxial STO/Si films with thicknesses of 25 nm (stoichiometric) a) and 50 nm (Sr-rich)) (b). The 50 nm thick STO film presents SrO segregations on the surface (b).  $\Theta/2\Theta$  XRD patterns of LN films on STO/Si films (pure and with SrO excess) and STO single crystal (c). The films were grown without Li<sub>2</sub>O excess or by introducing Li<sub>2</sub>O excess during the growth at 650 °C or 750 °C.

The reaction products and associated Gibbs energy of formation from LiNbO<sub>3</sub> and SrTiO<sub>3</sub> or their constituents (Li<sub>2</sub>O, Nb<sub>2</sub>O<sub>5</sub>, SrO, and TiO<sub>2</sub>), found by thermodynamic simulations using Factsage interface, are summarized in Table 1. One can note that LiNbO<sub>3</sub> phase is very stable and chemical interaction is not possible between LiNbO<sub>3</sub> and SrTiO<sub>3</sub>, TiO<sub>2</sub> or SrO. Li<sub>2</sub>O does not react with SrO, but its reactions with TiO<sub>2</sub> and SrTiO<sub>3</sub> are thermodynamically favourable. Ionic conductivity related to the mobility of Li<sup>+</sup> ions appears in LiNbO<sub>3</sub> above 300 °C. This makes possible chemical interactions between Li<sub>2</sub>O in LiNbO<sub>3</sub> and TiO<sub>2</sub>. Nb<sub>2</sub>O<sub>5</sub> does not interact with TiO<sub>2</sub>, but from thermodynamical point of view it might react with SrO in order to form

Sr<sub>2</sub>Nb<sub>2</sub>O<sub>7</sub>. The reactions which are thermodynamically favourable do not necessarily take place as their kinetics might be very slow. In order to check if the interaction between SrO and LiNbO<sub>3</sub> is possible, pure LiNbO<sub>3</sub> films were grown on 25 nm and 50 nm thick STO/Si templates, presenting pure STO and SrO/STO surfaces, respectively. The presence of Sr<sub>2</sub>Nb<sub>2</sub>O<sub>7</sub> phase was observed in LN films grown at 650 °C on the STO template with SrO excess, as indicated in the  $\Theta$ /2 $\Theta$  patterns by presence of the reflections on lower 2 $\Theta$  angle side of (200) STO reflection with 2 $\Theta$ =46.5° (Fig. 1 c). The Li<sub>2</sub>O reactivity with SrTiO<sub>3</sub> was verified by growing LN films with a slight excess of Li<sub>2</sub>O on pure 25 nm thick STO film at 750 °C. The parasitic reflection with 2 $\Theta$  angle in between those of (200) STO and (02 $\overline{2}$ 4) LN reflections was observed.

Table 1. Compounds and their Gibbs energy, G, of formation of reaction between LiNbO<sub>3</sub> and SrTiO<sub>3</sub>, or their constituents.

Compounds	Li <sub>2</sub> O	Nb <sub>2</sub> O <sub>5</sub>	LiNbO <sub>3</sub>
	(G [kJ.mol <sup>-1</sup> ])	(G [kJ.mol <sup>-1</sup> ])	(G [kJ.mol <sup>-1</sup> ])
SrO	No	Sr <sub>2</sub> Nb <sub>2</sub> O <sub>7</sub>	No
	compounds	(-1899)	compounds
TiO <sub>2</sub>	Li <sub>2</sub> TiO <sub>3</sub>	No	No
	(-1835)	compounds	compounds
SrTiO₃	Li <sub>2</sub> TiO <sub>3</sub> (-459) Sr <sub>4</sub> Ti <sub>3</sub> O <sub>10</sub> (-1565)	Sr <sub>2</sub> Nb <sub>2</sub> O <sub>7</sub> (-1899)	No compounds

This interaction was also identified between SrTiO<sub>3</sub> singlecrystal substrate and LiNbO<sub>3</sub> films with Li<sub>2</sub>O excess at 650 °C (Fig. 1 c). No parasitic phases were observed in pure LN films on pure STO films grown even at 750 °C confirming that pure STO and LN phases do not interact chemically (Fig. 1 c). This indicates that the compositions of LN and STO films have to be controlled with precision to avoid chemical interactions. The Θ/2Θ XRD patterns of LN films with a thickness of around 150 nm grown on pure 25 nm-STO/Si template by DLI-CVD at different temperatures ranging from 600 °C to 750 °C are given in Fig. 2 a. The films grown at different temperatures all present single LN phase composition and the films were homogeneous and continuous (Fig. 2b). Only  $\{01\overline{1}2\}$  family reflections of LN were observed in films grown at 750 °C indicating that LN films presented pure  $(01\overline{1}2)$ texture like in the case of epitaxial LN films grown on (100) STO single crystals. The  $(01\overline{1}2)$  orientation grows epitaxially also on (100)<sub>PC</sub> LAO (PC - pseudocubic unit cell settings, this orientation is equivalent to  $(01\overline{1}2)$  in standard hexagonal unit cell) and (100) LSAT substrates (Fig. 3). At lower deposition temperatures (600°C-700 °C), the (1123) growth orientation appeared and its volume percentage increased with the further decrease of the deposition temperature (Fig. 2 b). At deposition temperatures of 600-650 °C, the  $(11\overline{2}3)$  orientation

was dominant and the minor presence of c-axis orientation was observed, as well. The pure  $(11\bar{2}3)$  orientation growth was also identified in the case of  $(111)_{PC}$  (equivalent to (0006) planes in standard hexagonal unit cell) LAO substrates with in-plane lattice parameters of 2.683Å and 1.549 Å, as shown in Fig. 3. No reports on the  $(11\bar{2}3)$  LN orientation growth were found in literature.

The epitaxial growth of  $(01\overline{1}2)$  and  $(11\overline{2}3)$  orientations of LN on STO/Si was confirmed by measuring pole figures of (0006) reflection of LN (Fig. 4 c and d), which is expected to be tilted by 57° and 60° from the surface normal according to stereographic projections (Fig. 5) and the presence of four orientations of the c-axis due to formation of four types of growth domains, rotated by 90° in the substrate plane with respect to each other, due to fourfold symmetry of the substrate, respectively. In the four growth domains, the X-axis of  $(011\overline{2})$  LN and Y-axis of  $(11\overline{2}3)$  LN films are parallel to the [011],  $[0\overline{1}1]$ ,  $[0\overline{1}\overline{1}]$ , and  $[01\overline{1}]$  axes of SrTiO<sub>3</sub>. The inplane lattice parameters of  $(11\bar{2}0)$  and  $(30\bar{3}0)$  oriented LN and (100) STO are compared in Fig. 5. The lattice mismatch between the (011) family planes of STO and (11 $\bar{2}$ 0) and  $(30\overline{3}0)$  family planes of LN are -6.7% and 7.7%, respectively.  $(01\overline{14})$  and  $(11\overline{29})$  LN planes present better match (-0.9% and -4.2%) with (011) STO planes although the normal of these LN crystal planes are tilted by 5.1° and 1.8° from the surface  $(011\overline{2})$  and  $(11\overline{2}3)$  planes, respectively (Fig. 5).

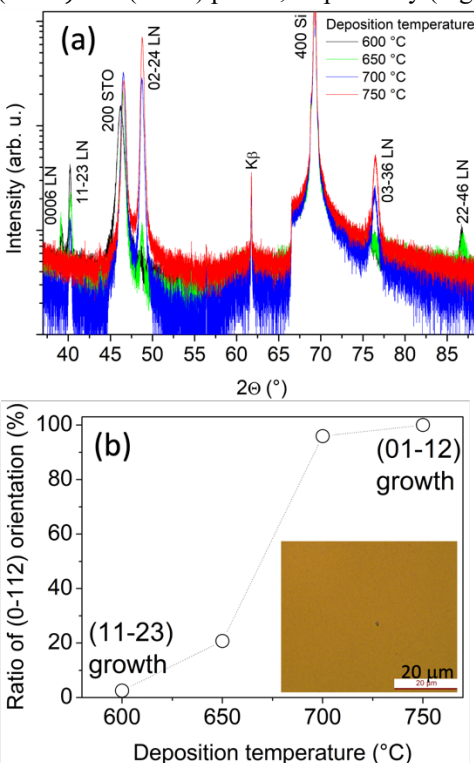


Figure 2.  $\Theta/2\Theta$  XRD patterns of epitaxial 150 nm thick LN film on (25 nm) STO/Si substrate, grown at different temperatures ranging from 600 °C to 750 °C (a). Dependence of the percentage of (01 $\overline{1}2$ ) orientation with respect to that of (11 $\overline{2}3$ ) orientation, estimated from reflection normalized intensities in  $\Theta/2\Theta$  XRD patterns, on the

deposition temperature and the optical image of LN film grown on STO/Si template at 750  $^{\circ}$ C (b).

The FWHMs of rocking curves of  $01\overline{1}2$  reflections of LN film on (100) STO single crystal and on (100) STO/Si template films were 1.9° and 2.6°, respectively (Fig. 4 a). The FWHMs of rocking curves of (100) reflections of corresponding STO substrate and STO/Si film were 0.25° and 1.4°, respectively. One can note the similar mosaicity of LN films grown on STO single crystal substrates and on epitaxial STO/Si templates. We would like to stress that the partial interdiffusion of STO layer with Si, silicates or SiO<sub>2</sub> formation at the interface should occur at LN deposition conditions [26-28], but it did not damage the epitaxial relationship between STO and LN layers, and the STO thickness of 25 nm was sufficient to protect LN/STO interface from Si pollution.

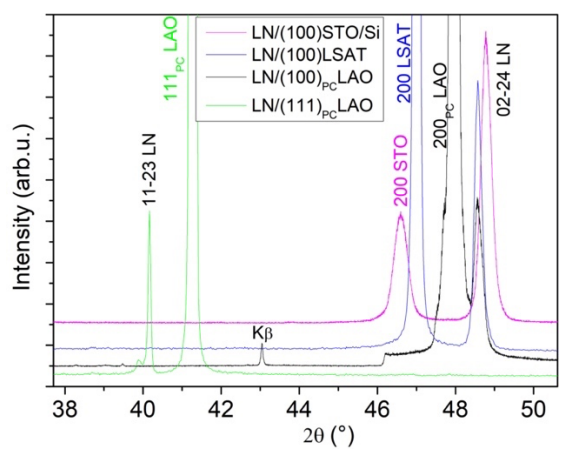


Figure 3  $\Theta/2\Theta$  XRD patterns of epitaxial 150 nm thick LN film on (25 nm) (100) STO/Si, (100) LSAT, (100)<sub>PC</sub> LAO and (111)<sub>PC</sub> LAO substrates.

The rocking curve FWHMs of  $11\overline{2}3$  LN and 200 STO reflections, display in Fig. 4 b were very close (1.54° and 1.61°, respectively), as well. One can note that the mosaicity of LN layer is directly defined by that of STO layers. The rocking curves consist of several components resulting in the large value of the global FWHM. This indicates that LN film grows with slightly tilted unit cell with respect to the surface plane of the substrate. As mentioned above, the normal of  $(01\overline{1}4)$  plane is tilted by 5.1° from the surface plane in the  $(01\overline{1}2)$  oriented LN crystal. According to the measured rocking curve, to match the  $(01\overline{1}4)$  plane with the  $(01\overline{1})$  STO plane, the normal of  $(01\overline{1}2)$  LN is tilted from the surface normal by around 3.35° by keeping the X-axis in the substrate plane. The tilted growth by 5° of  $(01\overline{1}2)$  oriented LN films was also observed on NdGaO<sub>3</sub> substrates [29].

The average roughness was around 3.2 nm as determined by means of atomic force microscopy. In order to introduce metal bottom electrode, the LN films were liberated from the STO/Si template by KOH etching and transferred to SiO<sub>2</sub>/Si substrate by using Au-Au bonding. The roughness of the transferred LN

film was 4.1 nm (Fig. 6). The coercive field of  $(01\overline{1}2)$  LN films was 85 kV.cm<sup>-1</sup>, indicating that Li<sub>2</sub>O composition in the film should be around 49.4 mol% as the congruent (48.34 mol%) composition of LN crystals presents coercive field of 207 kV/cm and nearly stoichiometric one (around 49.8 mol%) – 40.5 kV/cm [30].

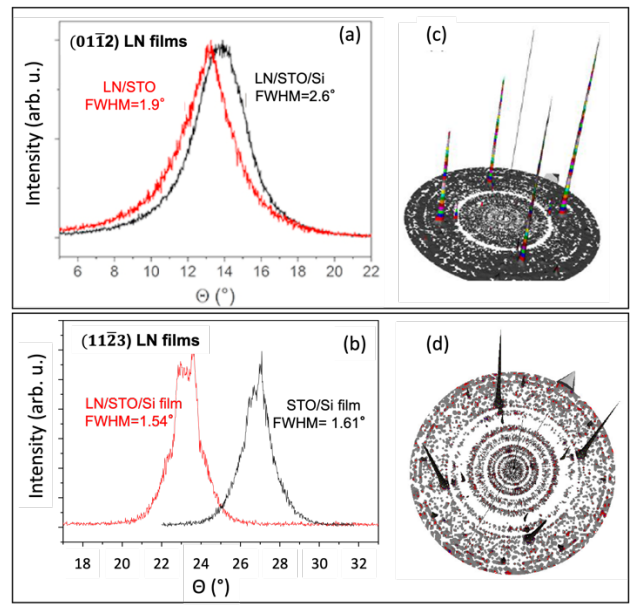


Figure 4. The rocking curves of  $01\overline{1}2$  reflection of LN film on STO single crystal and STO/Si template (a); the rocking curves of  $11\overline{2}3$  reflection of LN film and 200 reflection of STO/Si film (b), and pole figures of 0006 reflection (c and d) of epitaxial 150 nm thick LN film with  $(01\overline{1}2)$  and  $(11\overline{2}3)$  orientations on STO/Si templates, respectively.

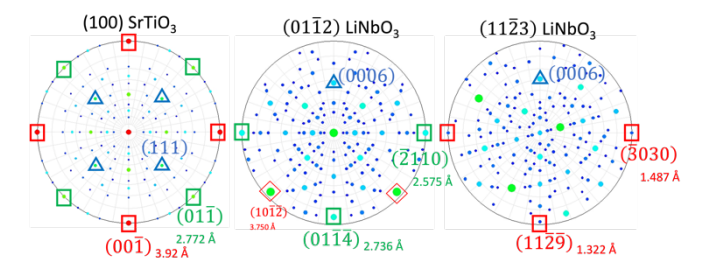


Figure 5. Stereographic projections of (100) STO, (01 $\overline{1}$ 2) and (11 $\overline{2}$ 3) LN orientations. The crystallographic planes perpendicular to the substrate plane are indicated by red and green squares. The in-plane lattice parameters are indicated, as well. The polarization axis (or (0006) plane) in LN structure and the equivalent (111) planes in cubic STO structure are indicated by blue triangles.

The transferred LN films were also used for the characterization by Raman spectroscopy in order to avoid the intense Si substrate signal, which was hindered thanks to reflectivity of Au electrode. The cross-polarized Raman spectra of transferred LN film and 36°Y -LN single crystal are compared in Fig. 6. According to the selection rules [21], mainly E(TO) modes are observed in both cases, although

more intense leakage of oblique modes (more details about the oblique modes can be found in Ref. [31]) is present in the case of LN film. This can be explained by the presence of the four growth domains and consequently grain boundaries introducing light scattering. In the case of Raman spectroscopy, it was not possible to estimate Li concentration with precision, as films presented four growth domains and the defective boundaries between these domains should affect the lifetime of the phonons and consequently contribute to the increase of the damping parameters of the Raman modes. Thus, Li<sub>2</sub>O concentration estimated by means of Raman spectroscopy can be assumed to be higher than 48.8 mol%, which confirms that  $(01\overline{1}2)$  LN films had Li concentration in between the congruent and stoichiometric ones.

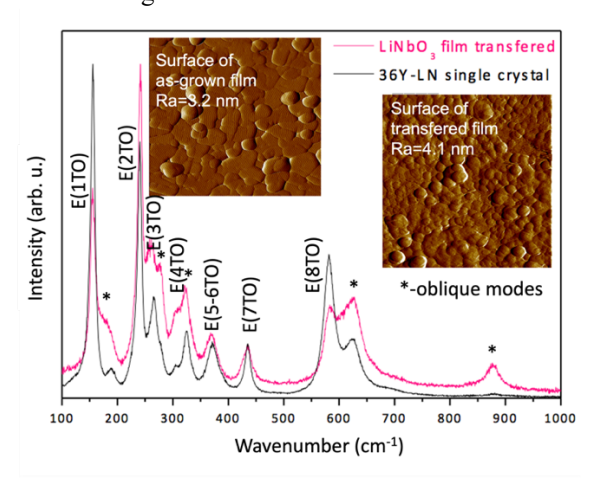


Figure 6. Comparison cross-polarized Raman spectra of transferred (0112) LN film and 36°Y-LN single crystal. The AFM error-signal images (2  $\square$ m x 2  $\square$ m) of the surface of as grown  $(01\overline{1}2)$  LN film on STO/Si and after its transfer process are given in insets. The roughness (Ra) was estimated from topographic images.

The thickness of  $(01\overline{1}2)$  LN films was around 150 nm and the films were crack-free. According to the XRD data (Fig. 2 a), the (0112) LN/STO/Si films deposited at 750 °C presented interplanar distances, reduced by 0.45%, indicating the presence of high tensile residual stresses in the substrate plane, which originated from one order of magnitude lower thermal expansion of Si substrate than that of X-axis of LN [24]. The wavenumber of E(6TO) mode of the transferred film was the same as that of LN single crystal indicating that the residual stresses were released thanks to the transfer process [24], and that it did not introduce any new stresses.

The piezoelectricity of  $(01\overline{1}2)$  oriented LN films on 25 nm STO/Si was confirmed by PFM measurements. The zones without piezoelectric response were not present. VPFM and LPFM images of (0112) LN layers on STO/Si show ferroelectric domains with components both in-plane and outof-plane, suggesting as-grown organization in polar domains (Fig. 7 a). Dark and bright areas correspond to regions in which the projection of the polarization vector in a direction perpendicular to the surface is in the opposite directions with (0112) orientations. Signal-to-noise ratio is better for LPFM images due to the polarization axis being tilted by around 57° from the surface normal. The ferroelectric domains had submicrometer lateral dimensions.

## 4. Discussion and concluding remarks

In the case of  $(01\overline{1}2)$  orientation of LN, the X-axis (perpendicular to  $(11\overline{20})$  plane in hexagonal unit cell) is in the substrate plane and Y-  $((10\overline{1}0)$ plane) and Z- axes ((0006)plane) are tilted by 33° and -57° from the surface normal (see stereographic projections in Fig. 5), respectively. Thus, this crystallographic orientation can be called as 32.76° rotated Y - X according to the IEEE Std-176 convention [6] (using XYZ orthogonal reference system, where Z- and X-axes are parallel to the c-axis and a-axis of the hexagonal cell). However, as explained above, the normal of  $(01\overline{1}2)$  LN films are tilted from the surface normal by around  $3.35^{\circ}$  in order to fit  $(01\overline{14})$ plane on the substrate. This adds additional tilt of the Y-axis from the substrate normal and the film orientation becomes  $36.11^{\circ}$  rotated Y - X (hereafter  $36^{\circ}$ Y-X). The (11 $\overline{2}$ 3) orientation of LN present Y-axis in the substrate plane and Xand Z- axes are tilted by 30° and -60° from the surface normal. Therefore, this orientation could be named 30°X-Y, as well.

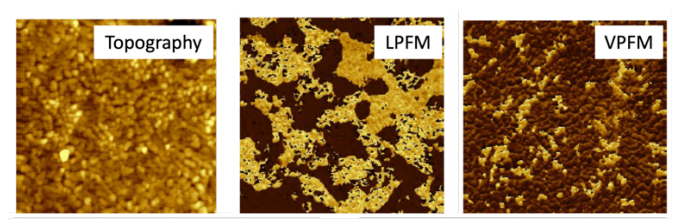


Figure 7. 5  $\square$ m x 5  $\square$ m topography (30 nm from black to white), *LPFM* and *VPFM* phase images obtained on  $(01\overline{1}2)$ LN/25nmSTO/Si samples. In phase images, dark and bright regions correspond to an opposite direction of the polarization projected on the vertical axis (VPFM) or horizontal axis perpendicular to the AFM lever (LPFM).

In the case of the BAW devices, the electromechanical coupling factor of the longitudinal wave,  $K_L^2$ , was calculated for Z, 36°Y-X and 30°X-Y LN orientations (Table 2):

$$K_L^2 = \frac{e_{33}^2}{\varepsilon_{22}^S c_{22}^D} Eq.$$

 $K_L^2 = \frac{e_{33}^2}{\varepsilon_{33}^2 c_{33}^D} \ Eq. \ I$  Where  $e_{33}$  is a stress piezoelectric constant,  $c_{33}^D$ - an elastic stiffness at constant dielectric displacement,  $\varepsilon_{33}^S$  – a permittivity at constant strain. 36°Y-X and 30°X-Y LN offer considerably higher electromechanical coupling factor (24.3% and 10.9%, respectively) than that of Z-axis oriented films (5.4%), which was so far considered for the grown LN films in the literature [15].

Despite being less piezoelectrically coupled than the X-cut orientation studied in the case of film by ion slicing techniques, BAW resonators using 36°Y LN operate on pure longitudinal wave [10] and not on a mix of two close shear waves as with X-cut or a mixture of shear and longitudinal waves of 30°X-Y orientation. Hence, the 36°Y-X orientation may offer a parasitic-free BAW resonator or filter response. Moreover, the direct growth of LN films enables application of LN films with thicknesses below 250 nm which opens the possibility for the BAW devices with operational frequencies above 10 GHz. The 36°Y-LN films with four co-existing orientations in the plane cannot be applied in devices based on SAW or Lamb waves, requiring proper propagation direction, but can be used for BAW devices using thickness excitation.

Table 2. Comparison of the electromechanical coupling factor of longitudinal waves,  $K_L^2$ , for Z-, 36°Y-X and 30°X-Y orientations of LN. The coefficients are given for the single-crystal material [32] as where is no averaging effect due to four growth domains rotated in the substrate plane for the 33 coefficients.  $\varepsilon_0$  is the permittivity of free space (8.85 pF m<sup>-1</sup>).

Film orientation	e' <sub>33</sub> (C.m <sup>-2</sup> )	$\varepsilon_{33}^{\prime S}/\varepsilon_{0}$	c' <sup>D</sup> <sub>33</sub> (GPa)	K <sub>L</sub> <sup>2</sup> (%)
Z	1.77	27.3	241	5.4
36°Y-X	4.63	39.5	252	24.3
30°X-Y	3.01	41.2	229	10.9

In the case of actuation or vibrational energy harvesting applications, 31 mode excitation mode can be considered. Its figure of merit for the structures using piezoelectric thin films,  $FoM_{31.film}^T$ , can be expressed as follows

$$FoM_{31,film}^{T} = \frac{e_{31,film}^{2}}{\varepsilon_{33,film}^{T}} Eq. 2$$

Where  $e_{31,film}$  is a stress piezoelectric constant and  $\varepsilon_{33,film}^T$  – a permittivity at constant stress of the film, which differ from those of the single crystal due to the substrate clamping effect [14]. The comparison of  $FoM_{31,film}^T$ , piezoelectric and permittivity coefficients for Z,  $36^{\circ}\text{Y-X}$  and  $30^{\circ}\text{X-Y}$  orientated films with four growth domains in the substrate plane are given in the Table 3.  $36^{\circ}\text{Y-X}$  orientation presents higher performance than Z or  $30^{\circ}\text{X-Y}$  orientations and offers the  $FoM_{31,film}^T$  of 27.4 kJ.cm<sup>-3</sup> which is comparable to that of the standard PZT films (28.8 kJ/cm<sup>3</sup>) and higher by a factor of 2 than those of lead-free ZnO and AlN films (13.1 kJ.cm<sup>-3</sup> and  $10.3 \text{ kJ.cm}^{-3}$ ) available at industrial scale [14]. This indicates high potential of  $36^{\circ}\text{Y-LN}$  films for the lead-free MEMS scale actuators, energy harvesters and sensors.

Although, these 36°Y LN films on Si are very promising for BAW and other electro-active applications, additional effort is needed to integrate these films to the standard TFBAR or SMR (solidly mounted resonators)-BAW structures based on the electrode/sacrificial layer/Si or electrode/Bragg mirrors/Si or on the bottom electrode. This can be done by developing specific epitaxial bottom electrodes, Bragg mirrors and sacrificial layers compatible with epitaxial 36°Y LN film growth or more simply by using the layer transfer technique including wafer bonding and etching of sacrificial layers

enabling the integration with standard BAW structures. Moreover, we have demonstrated that LN film can be liberated easily from the STO/Si template by selective KOH etching.

To summarize, the epitaxial growth of 36°Y-LN films by DLI-CVD at 750 °C on Si substrates by using epitaxial STO layers, grown by MBE, has been demonstrated. Although STO and LN do not interact chemically at this temperature, particular attention has to be given to avoid SrO excess on the STO surface and Li<sub>2</sub>O excess during the LN growth which induce the chemical interaction and the formation of parasitic phases. High deposition temperature (750°C) of LN films is an essential factor to avoid epitaxial growth of  $(11\overline{2}3)$ orientation and to obtain pure  $(01\overline{1}2)$  orientation. At this deposition temperature the interdiffusion between STO and Si takes place, but 25 nm thick STO layer is sufficient to protect epitaxial growth at LN/STO interface. The piezoelectricity of LN films was confirmed by PFM measurements and the ferroelectric domain inversion was attained at 85 kV.cm<sup>-1</sup> as expected for the LN with intermediate Li<sub>2</sub>O composition between congruent and stoichiometric ones. According to the simulation, 36°Y-LN films on Si could offer an electromechanical coupling of 24.3 % for BAW devices based on pure longitudinal wave. This could open new opportunities for development of wide band and high frequency BAW filters with frequencies above 10 GHz in line with 6<sup>th</sup> generation (6G) telecommunication applications. The 36°Y-LN films also present the figure of merit comparable to that of PZT and a new possibility for the developments of the lead-free MEMS actuators, energy harvesters and sensors in addition to other integration opportunities with epitaxial Perovskite platforms on Si.

Table 3. Comparison of the figure of merit,  $FoM_{31,film}^T$ , for Z-,  $36^\circ Y$ -X and  $30^\circ X$ -Y orientated of LN films with four orientations in the substrate plane. The efficient piezoelectric and permittivity coefficients,  $e_{31}'$  and  $\varepsilon_{33}^{'T}$ , were estimated by using the single-crystal LN properties [32] and applying the fourfold symmetry axis along the growth orientation. The effect of the substrate clamping on the film permittivity,  $\varepsilon_{33,film}'$ , and stress piezoelectric coefficient,  $e_{31,film}'$  was estimated [14].  $\varepsilon_0$  is the permittivity of free space (8.85 pF  $m^{-1}$ ).

Growth orientation	e' <sub>31</sub> (C.m <sup>-2</sup> )	e' <sub>31,film</sub> (C.m <sup>-2</sup> )	$\varepsilon'_{33}^{T}$ $/\varepsilon_{0}$	$\varepsilon'^{T}_{33,film}$ $/\varepsilon_{0}$	$FoM_{31,film}^T$ (kJ.cm <sup>-3</sup> )
Z	0.3	-0.2	28.9	28.8	0.2
36°Y-X	-1.69	-3.66	70.3	55.4	27.4
30°X-Y	-1.91	-2.4	72.7	63.3	10.3

#### Acknowledgements

Authors would like to thank Prof. Paul Muralt for the derivation of the equation of the electromechanical coupling for the longitudinal wave. This work was supported by the French RENATECH network and its FEMTO-ST technological facility, Bourgogne Franche-Comté region, the French national ANR projects LINKS ANR20-CE08-0025 LiLit ANR-16-CE24-0022-011, and the graduate school EUR EIPHI contract ANR-17-EURE-0002. RB and GSG are grateful of MBE technical support of P. Regreny, C. Botella, and J.B. Goure from Nanolyon technology platform.

# Data availability statement

The data that support the findings of this study are available upon reasonable request from the authors.

## References

- [1] Liu Y, Cai Y, Zhang Y, Tovstopyat A, Liu S and Sun C 2020 Micromachines 11 (7) 630
- [2] www.docomo.ne.jp
- [3] Muralt P, Antifakos J, Cantoni M, Lanz R a ndMartin F 2005 *IEEE Ultrasonics Symp.* 315
- [4] Akiyama M, Kamohara T, Kano K, Teshigahara A, Takeuchi Y and Kawahara N 2009 Adv. Mater. 21 (5) 593-6
- [5] Matloub R, Hadad M, Mazzalai A, Chidambaram N, Moulard G, Sandu C S, Metzger T and Muralt P 2013 Appl. Phys. Lett. 102 152903
- [6] Meitzler A H, Berlincourt D, Coquin G A, Welsh III F S, Tiersten H F and Warner A W 1978 IEEE Standard on Piezoelectricity, ANSI/IEEE Std Series 176-1978, Institute of Electrical and Electronics Engineers, New York, USA
- [7] Warner A W, Onoe M and Coquin G A 1967 J. Acoust. Soc. Am. 42 (6) 1223
- [8] Reinhardt A, Benaissa L, David J-B, Lamard N, Kovacova V, Boudou N and Defaÿ E 2014 Proc. – IEEE Ultrason. Symp. 773
- [9] Pijolat M, Loubriat S, Queste S, Mercier D, Reinhardt A, Defaÿ E, Deguet C, Clavelier L, Moriceau H, Aïd M and Ballandras S 2009 Appl. Phys. Lett. 95 182106
- [10] Reinhardt A, Bousquet M, Joulie A, Hsu C-L, Delaguillaumie F, Maeder-Pachurka C, Enyedi G, Perreau P, Castellan G and Lugo J 2021 Proceedings EFTF-IFCS
- [11] Yang Z, Zhou S, Zu J and Inman D J 2018 Joule 2 (4) 642–697
- [12] Evans D 2011 The Internet of Things. How the Next Evolution of the Internet Changing Everything (CISCO White Paper)
- [13] Clementi G, Ouhabaz M, Margueron S, Suarez M A, Bassignot F, Gauthier-Manuel L, Belharet D, Dulmet B, Bartasyte A 2021 Appl. Phys. Lett. 119 (1) 013904
- [14] Bartasyte A, Clementi G, Micard Q, Labbaveettil I, Moreira A.S.L, Boujnah S, Ouhabaz M, Verma A, Malandrino G, Mathur S, B. Dulmet B and Margueron S 2023 J. Micromechanics and Microengineering 33 053001
- [15] Bartasyte A, Margueron S, Baron T, Oliveri S and Boulet P 2017 Adv. Mater. Interfaces 4 (8) 1600998
- [16] Iwashita S, Higuchi T and Miyazawa H 2006 Patent US7005947 B2
- [17] Kadota M, Ogami T, Yamamoto K, Tochishita H and Negoro Y 2010 IEEE TUFFC 57 (11) 2564

- [18] Kadota M, Suzuki Y and Ito Y 2010 *IEEE Int. Ultrasonics Symp.*
- [19] Saint-Girons G, Bachelet R, Moalla R, Meunier B, Louahadj L, Canut B, Carretero-Genevrier A, Gazquez J, Regreny P, Botella C, Penuelas J, Silly M G, Sirotti F and Grenet G 2016 Chem. Mater. 28 (15) 5347–5355
- [20] Niu G, Vilquin B, Penuelas J, Botella C, Hollinger G and Saint-Girons G 2011 J. Vacuum Science & Technology B 29 (4) 041207
- [21] Bartasyte A, Plausinaitiene V, Abrutis A, Stanionyte S, Margueron S, Kubilius V, Boulet P, Huband S and Thomas P. A. 2015 Mater. Chem. Phys. 149 622
- [22] Bartasyte A, Plausinaitiene V, Abrutis A, Stanionyte S, Margueron S, Boulet P, Kobata T, Uesu Y and Gleize J 2012 J. Phys.: Condens. Matter 25 205901
- [23] Margueron S, Bartasyte A, Glazer A M, Simon E, Hlinka J, Gregora I and Gleize J 2012 J. Appl. Phys. 111 104105
- [24] Bartasyte A, Plausinaitiene V, Abrutis A, Murauskas T, Boulet P, Margueron S, Gleize J, Robert S, Kubilius V and Saltyte Z 2012 Appl. Phys. Lett. 101 122902
- [25] Bale C W, Bélisle E, Chartrand P, Decterov S A, Eriksson G, Hack K, Jung I-H, Kang Y-B, Melançon J, Pelton A D, Robelin C and Petersen S 2009 Calphad 33 (2) 295-311
- [26] Goncharova L, Starodub D, Garfunkel E, Gustafsson T, Vaithyanathan V, Lettieri J and Schlom D 2006 J. Appl. Phys. 100 014912
- [27] Lee K H, Saada S, Arnault J-C, Moalla R, Saint-Girons G, Bachelet R, Bensalah H, Stenger I, Barjon J, Tallaire A and Achard J 2016 Diamond and Related Materials 66 67-76
- [28] Vila-Fungueiriño J M, Bachelet R, Saint-Girons G, Gendry M, Gich M, Gazquez J, Ferain E, Rivadulla F, Rodriguez-Carvajal J, Mestres N, Carretero-Genevrier A 2015 Frontiers in Physics 3 38
- [29] Tagliente M A, De Caro L, Sacchetti A, Tapfer L, Balestrino G, Medaglia P G, Tebano A and Tucciarone A 2000 J. Cryst. Growth 216 335
- [30] Gopalan V, Dierolf V and Scrymgeour D A 2007 Annu. Rev. Mater. Res. 37 (1) 449–489
- [31] Bartasyte A, Margueron S, Glazer A M, Simon E, Gregora I, Huband S and Thomas P A 2019 *Physical Review B* 99 (9) 094306
- [32] Kovacs G, Anhorn M, Engan H E, Visintini G and Ruppel C C W 1990 Ultrasonics Symposium Proceedings 435–438